Journal of Materials Chemistry B

ROYAL SOCIETY OF CHEMISTRY

PAPER

View Article Online
View Journal | View Issue

Cite this: J. Mater. Chem. B, 2025, 13, 11821

A multifunctional electrospun nanofiber/hydrogel-based pro-healing bilayer dressing as a next generation biomaterial for skin wound care

Dimpy Bhardwaj,[a] Vatan Chawla,[b] Vanshika Nandwani,[a] Yashika Thakur,[b] Yashveer Singh [b] and Garima Agrawal *[a]

Infectious wounds present a significant challenge in healthcare due to the delay in wound healing and associated processes. Improper use of antibiotics makes this situation even worse due to antibiotic resistance. To meet the critical requirements of healing infectious wounds, we report a bilayer dressing (BL) that combines a hydrogel-based layer and an electrospun nanofiber-based layer together to mimic the dermal and epidermal architecture of normal skin. The bilayer dressing is fabricated by combining a chitosan/gelatin nanofiber-based layer (NF) with an ursodeoxycholic acid drug (UDC) and carbon dot (CD) loaded hydrogel (UDC/CDs/H-Gel). The hydrogel is fabricated by Schiff base-based crosslinking of quaternized chitosan (QCS) and oxidized alginate (OA). The integration of NF with UDC/CDs/H-Gel leads to ~45% increment in tensile strength and ~48% increment in elongation at break. The BL exhibits a swelling of ~400% in 36 h, a porosity of ~75%, and an antioxidant activity of ~93%. Moreover, as compared to individual NF and hydrogel layers, the BL shows good reactive oxygen species (ROS) scavenging behavior, good hemocompatibility (~4.5% hemolysis), good hemostatic potential, enhanced cell proliferation ability (130% cell viability of L929 cells), and excellent antibacterial activity with 92% and 88% bactericidal efficacy against *E. coli* and *S. aureus*, respectively. The wound healing ability of the BL is further evaluated *via* scratch assay demonstrating ~97% wound closure. Overall, the BL possesses multifunctionality and presents itself as a potential candidate for accelerated wound healing.

Received 7th April 2025,
Accepted 15th August 2025

DOI: 10.1039/d5tb00800j

rsc.li/materials-b

1. Introduction

Skin is the outermost layer of the body that directly comes into contact with the environment, and it is one of the most vulnerable tissues due to its closest interaction with the external factors. For minor injuries, skin can heal itself over time *via* a complex wound healing process, which includes four overlapping and coordinated stages, namely hemostasis, inflammation, proliferation, and remodeling.[1,2] This process helps in restoring the overall physiology and function of skin but any kind of disruption in this continuous healing process may lead to chronic wounds having persistent inflammation and impaired healing. Various factors like diabetes, infection, and stress interfere with the wound healing process, resulting in higher occurrence of chronic wounds.[2,3] According to a study, wound care related expenditure is estimated to be around $28–$97 billion annually, resulting in heavy financial burden in the medical sector.[4]

Gauze is the most traditional and inexpensive alternative to treat the wound but the need for its frequent replacement may lead to trauma and mechanical debridement, and the leftover fiber may trigger the immune system causing granuloma formation.[5] To address this challenge, advanced wound dressings have been designed based on "the moist wound healing theory" given by Prof. Winter in 1962.[6] An ideal wound dressing is expected to be biocompatible and non-inflammatory; retain moisture; and have sufficient mechanical strength to maintain the structural integrity. It should be capable of performing the required biochemical actions for supporting the healing process.[7]

Various monolayer wound dressings based on hydrogels, electrospun fibers, foams, and hydrocolloids have been investigated to address the challenges associated with gauze.[8–11] To design the polymer matrix for these wound healing dressings, natural polymers are an attractive choice owing to their inherent biocompatibility and biodegradability.[12–14] These natural polymers, such as chitosan, alginate, and gelatin, can be extracted from natural resources and possess different functional groups, which can be used for post-modifications as per the requirements.[15–17] In recent years, hydrogels loaded with nanomaterials have attracted considerable interest for wound healing applications.[18–21] In this context, silver-based nanomaterials have been widely utilized for

[a] School of Chemical Sciences and Advanced Materials Research Centre, Indian Institute of Technology Mandi, Mandi, 175075, Himachal Pradesh, India. E-mail: garima@iitmandi.ac.in; Tel: +91-1905-267827
[b] Department of Chemistry, Indian Institute of Technology Ropar, Rupnagar, 140001, Punjab, India

the treatment of infected wounds due to their strong and broad-spectrum antibacterial efficacy.[22] However, apprehensions regarding their cytotoxic effects on host tissues and the risk of inducing allergic reactions have limited their utilization.[23] In recent years, carbon dots have emerged as an alternative active component owing to their exceptional biocompatibility, intrinsic antioxidant properties, adjustable surface functionalities, and antibacterial efficacy combined with minimum toxicity risk.[24,25] For example, Zaffar *et al.* developed a urea/citric acid-based carbon dot and rose-petal-derived extracellular vesicle loaded injectable hydrogel with intrinsic antibacterial activity.[26] Qu *et al.* reported MXene/carbon dot nanocomposites with anti-inflammatory and NIR-triggered antibacterial effects.[27] Furthermore, Li *et al.* incorporated peroxidase-like copper-doped carbon dots into a chitosan/dextran-based hydrogel for stimuli-responsive biofilm disruption and enhanced healing.[28] The above mentioned systems have required features for wound healing applications exclusive of each other, but none of the systems independently attain the complete set of physical and biological efficacy when used as an individual layer.

The development of porous dressings with a layered gradient can be considered as a step further, as it mimics the skin anatomy, which has epidermis and dermis.[29] In this regard, bilayer (BL) dressings consisting of an electrospun fiber-based layer and a hydrogel-based layer have emerged as a potential alternative.[4,30–32] Here, the electrospun fiber-based layer provides a dense structure with small pores to maintain the breathability and provide protection from bacterial invasion, which is similar to epidermis,[4,33] whereas the loose 3D porous structure of the hydrogel layer can mimic the dermal layer by providing a moist environment and supporting cell growth along with offering other required biochemical functions.[4,34] However, relatively limited studies have been performed so far on bilayer dressings. Bilayer dressings based on cellulose acetate nanofibers with a collagen hydrogel,[35] poly(L-lactic acid) (PLLA) nanofibers with a chitosan/gelatin hydrogel,[4] PLLA/chitosan/poly(3-hydroxybutyrate-*co*-3-hydroxyvalerate) (PHBV) nanofibers with a chitosan/gelatin hydrogel,[36] keratin nanofibers with a polyacrylic acid hydrogel,[32] and polyvinyl alcohol/alginate nanofibers with a chitosan hydrogel[37] are some examples that have been reported in the literature. These bilayer dressings generally lack the capability of performing multiple actions together like antioxidant, antibacterial, controlled release of active components, hemostasis, and reactive oxygen species (ROS) scavenging, which are crucial for the healing of infectious wounds. Therefore, it is the need of the hour to focus on multifunctional bilayer dressings for achieving faster healing of bacteria-infected wounds and to improve their prospects in real-life applications.

To address the research gap of desired multifactorial physical and biological properties in a single dressing, based on the above-mentioned knowledge, we hypothesized to combine chitosan/gelatin-based electrospun fibers with an ursodeoxycholic acid drug (UDC) and citric acid-based carbon dot (CD) loaded hydrogel. UDC shows strong potential for promoting wound healing due to its ability to suppress NF-κB signaling, along with its anti-inflammatory effects and tissue regeneration feature.[38,39] Here, the polymeric matrix with UDC can help in wound exudate absorption, cell adhesion and proliferation, and hemostasis, while chitosan and CDs can offer antioxidant, antibacterial, and ROS scavenging features. Also, good interfacial adhesion of nanofibers and hydrogel-based layers can offer enhanced mechanical strength to the dressing. Based on this hypothesis, in the current work, we have developed bilayer dressings fabricated by combining chitosan/gelatin-based electrospun fibers with a quaternized chitosan/alginate-based hydrogel for enhanced wound healing. The epidermis-mimicking layer was prepared by electrospinning the solution of chitosan and gelatin, whereas the dermis-mimicking hydrogel layer was prepared by Schiff base-based crosslinking between quaternized chitosan (QCS) and oxidized alginate (OA). The hydrogel layer was further loaded with CDs and UDC, thus providing the antioxidant, antibacterial, and cell growth promoting features to the bilayer dressing. This bilayer dressing (BL) was investigated for its various physicochemical and active properties. The wound healing ability of the BL was investigated through *in vitro* scratch assay, which revealed a substantial decrease in the scratch area. Owing to its biochemical functions, the developed bilayer dressing demonstrates great potential as a dressing material for enhanced wound healing.

2. Materials and methods

2.1. Materials

Chitosan (600–800 kDa mol wt), sodium hydroxide (NaOH, 97%), 3-(4,5-dimethylthiazol-2-yl)-2,5-diphenyl-2*H* tetrazolium bromide (MTT), Dulbecco's modified Eagle's medium (DMEM), fetal bovine serum (FBS), Triton-X and RPMI were purchased from Thermo Fisher Scientific, India. Gelatin Type A (total nitrogen ≥15.50%, protein: 70–90%) and Luria broth were purchased from HiMedia, India. Sodium alginate (Alg, ∼200 kDa mol wt) was acquired from CDH, India. Sodium metaperiodate (99.8%), phosphate buffered saline (PBS), and ethylene glycol (99.5%) were purchased from Loba Chemie, India. Glycidyl trimethyl ammonium chloride (*ca.* 80% in water), ursodeoxycholic acid (UDC, >98.0%), and the 2,2-diphenyl-1-picrylhydrazyl radical (DPPH) were acquired from TCI chemicals, India. Citric acid (≥99.0%) and 2′,7′-dichlorodihydrofluorescein diacetate (H_2DCFDA, ≥97%) were acquired from Merck Life Science, India. Acetic acid (99.0%), *p*-nitrophenylhydrazine (99%), dimethylformamide (DMF, 99.5%), and ethylene diamine (99%) were purchased from SRL, India. *S. aureus* (MTCC 7443) and *E. coli* (MTCC 1687) were obtained from CSIR – IMTECH, Chandigarh. Fresh human blood was collected from healthy humans, following the guidelines approved by the Institutional Biosafety Committee (#07/2021-II/IIT/IEC).

2.2. Fabrication of citric acid-based carbon dots (CDs)

CDs were prepared using citric acid as the source of carbon *via* a one-step hydrothermal method.[40,41] Briefly, 2.5 g of citric acid and 2.5 mL of ethylene diamine were mixed together in 50 mL of water, and the solution was transferred to a Teflon lined

stainless steel reactor (100 mL). The reaction was carried out at 180 °C for 12 h. Next, the sample was centrifuged at 8000 rpm for 10 min and then filtered through a 0.22 μm membrane filter. Finally, the sample was dialyzed against water for 48 h using a 1 kDa dialysis membrane and stored at room temperature.

2.3. Fabrication of a chitosan/gelatin electrospun nanofiber-based layer (NF)

To fabricate NF, 8% w/v chitosan solution was prepared in 3 mL of 80% acetic acid and 30% w/v gelatin solution was prepared separately in 6 mL of 80% acetic acid. Both solutions were mixed and kept for overnight stirring until the mixture was homogenous and viscous, and this uniform solution was electrospun over the cylindrical collector positioned 15 cm away, perpendicular to a needle. The needle was attached to the positive terminal of a high-voltage direct current power supply and nanofibers were collected by applying an electric potential of 16 kV to the polymer solution, with a flow rate of 0.4 mL h^{-1}.

2.4. Formation of the bilayer dressing (BL)

To fabricate the BL, QCS and OA were utilized to generate a Schiff base linkage-based hydrogel layer. QCS was prepared according to the methodology reported by Negi *et al.*,[42] and the degree of quaternization (~23%) was estimated by conductometric titration using the following formula:

$$\frac{C_{AgNO_3} \cdot V_{AgNO_3}}{m} = \frac{DS}{DS \cdot M_3 + (1 - DS - DA) \cdot M_1 + DA \cdot M_2} \quad (1)$$

where C_{AgNO_3} = $AgNO_3$ concentration, V_{AgNO_3} = volume of $AgNO_3$ solution, m = mass of QCS used for titration, DS is the degree of quaternization, DA is the acetylation degree of chitosan, M_1 = glucosamine molecular weight, M_2 = *N*-acetyl glucosamine molecular weight, and M_3 = GTMAC molecular weight.

OA was synthesized using the previously described protocol by Dhiman *et al.*,[43] and the hydroxylamine hydrochloride assay was used to calculate percent oxidation (~71%) using the following formula:

$$\frac{\text{Mole of CHO}}{\text{Mole of uronic acid}} = V_{NaOH} \times 0.1 \text{ mol L}^{-1} \times \frac{198 \text{ g mol}^{-1}}{M_{sample}} \times 100 \quad (2)$$

Here, V_{NaOH} represents the volume of NaOH consumed during titration and M_{sample} denotes the mass of oxidized alginate used in the titration.

In the next step, 150 μL of QCS solution and 150 μL of OA solution in DI water were mixed homogeneously by maintaining a QCS : OA ratio of 3 : 5 (w/w). Next, CDs (1 : 80 w/w relative to hydrogel forming solution) and a methanolic solution of UDC (1 : 10 w/w relative to hydrogel forming solution) were added to the aforementioned solution.

Finally, the bilayer dressing was prepared by using the vacuum filtration method, where NF was kept in the Buchner funnel and hydrogel forming solution was poured onto it. It was observed that the hydrogel layer was formed within 2 min at room temperature, and after applying vacuum, a strong interface between the two layers was formed, which can be clearly visualized using a SEM. The BL was characterized using FT-IR spectroscopy, SEM and a universal testing machine (UTM).

For comparative studies, the following hydrogel samples were prepared: (a) the unloaded QCS/OA hydrogel (H-Gel) and (b) the UDC and CD loaded QCS/OA hydrogel (UDC/CDs/H-Gel). The loading efficiency of the UDC drug was calculated as follows:[44]

$$\%\text{ Loading efficiency (LE)} = \frac{\text{Amount of drug added}}{\text{Weight of film}} \times 100 \quad (3)$$

2.5. Physicochemical characterization and *in vitro* studies

The experimental details of physicochemical characterization, UDC release studies, antioxidant and antibacterial studies, and cell studies are given in the SI.

2.6. Instrumentation and characterization

The details of instrumentation and characterization are given in the SI.

3. Results and discussion

In this work, the bilayer dressing (BL) was designed to deal with the challenges related to infectious wounds while keeping the bilayer structure of skin in mind. A chitosan/gelatin electrospun nanofiber-based layer (NF) was prepared separately using an electrospinning method. Next, the bilayer dressing (BL) was developed by pouring the CD and UDC containing hydrogel forming solution on NF under vacuum filtration (Scheme 1). Here, the hydrogel layer was formed on top of NF and a strong interface was formed between NF and the hydrogel layer resulting in a bilayer structure, offering multifactorial pro-healing features for enhanced skin wound healing.

3.1. Characterization of a chitosan/gelatin electrospun nanofiber-based layer (NF)

A chitosan/gelatin electrospun nanofiber-based layer was fabricated *via* an electrospinning method. Comparative FT-IR spectra of chitosan, gelatin, and NF are shown in Fig. S1 in SI. It can be seen that all the peaks of gelatin and chitosan were present in the FT-IR spectrum of NF, confirming the presence of both the biopolymers in the nanofibers. These fibers are expected to have hydrogen bonding interactions between $-NH_2$, –C═O, and –OH groups of both chitosan and gelatin. Similar interactions have also been reported in other chitosan/gelatin-based systems in the literature.[45] Fabricated NF was also characterized using SEM and the results have been discussed later in Section 3.4.

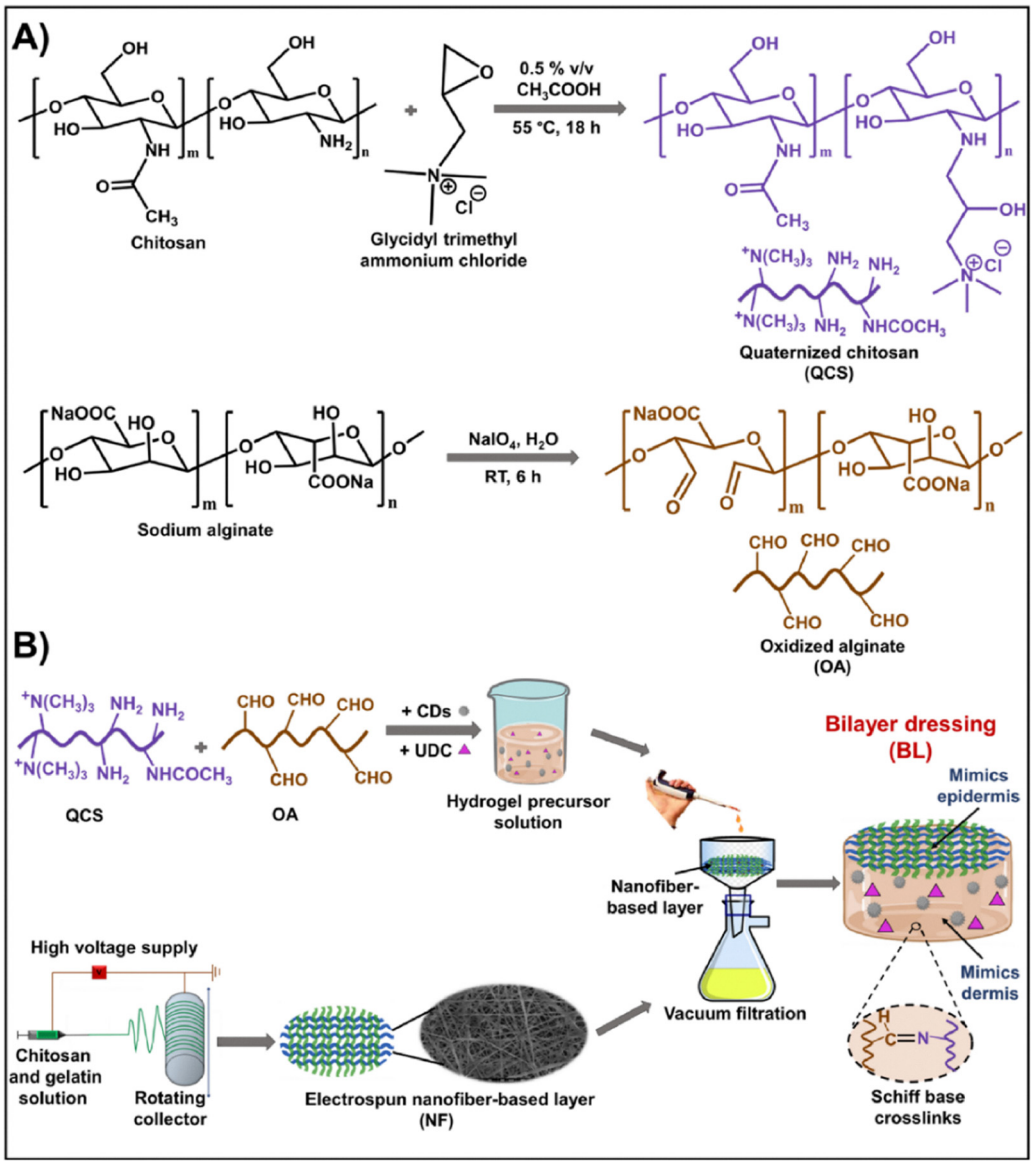

Scheme 1 (A) Synthesis of quaternized chitosan (QCS) and oxidized alginate (OA). (B) Fabrication of a multifunctional electrospun nanofiber/hydrogel-based pro-healing bilayer dressing (BL) for infectious wounds.

3.2. Characterization of citric acid-based carbon dots (CDs)

CDs were prepared *via* a one-step hydrothermal method utilizing citric acid as a carbon source. CDs displayed a size of 28 nm with the polydispersity index (PDI) of 0.3 as measured by dynamic light scattering (Fig. S2). The zeta potential of CDs was −23.6 mV, indicating the colloidal stability of CDs *via* strong electrostatic repulsion (Fig. S3). The TEM image of CDs showed their homogeneous distribution (Fig. 1A) with an average size of approximately 4.2 ± 1.9 nm (Fig. 1B).

The FT-IR spectra of citric acid and CDs are shown in Fig. S4 in SI. The FT-IR spectrum of citric acid showed peaks at 3492 cm^{-1} (O–H stretching) and 3280 cm^{-1} (O–H stretching of the carboxylic group), 2892 cm^{-1} (C–H stretching), and 1697 cm^{-1} (C=O stretching), whereas the FT-IR spectrum of CDs displayed peaks at 3284 cm^{-1} (O–H and N–H stretching), 2930 cm^{-1} (C–H stretching), 1540 cm^{-1} (asymmetric C–O stretching of the carboxylate group), and 1370 cm^{-1} (symmetric C–O stretching of the carboxylate group). A peak at 1580 cm^{-1} (N–H bending) was also observed in the case of CDs, which was attributed to the nitrogen functionalities on CDs.[43,46]

Moreover, X-ray photoelectron spectral (XPS) analysis was performed to detect the surface components and functional groups in CDs. The XPS survey spectrum of CDs displayed the presence of carbon, oxygen, and nitrogen elements in CDs (Fig. S5A). The high-resolution spectrum of C 1s exhibited three peaks (Fig. S5B) at 288, 286.3, and 284.7 eV, which were ascribed to C=O, C–N, and C–C, respectively.[47] The N 1s spectrum indicated the presence of alkyl ammonium groups (401.8 eV) and N–H (399.6 eV) groups, thus demonstrating the presence of nitrogen containing functionalities on CDs

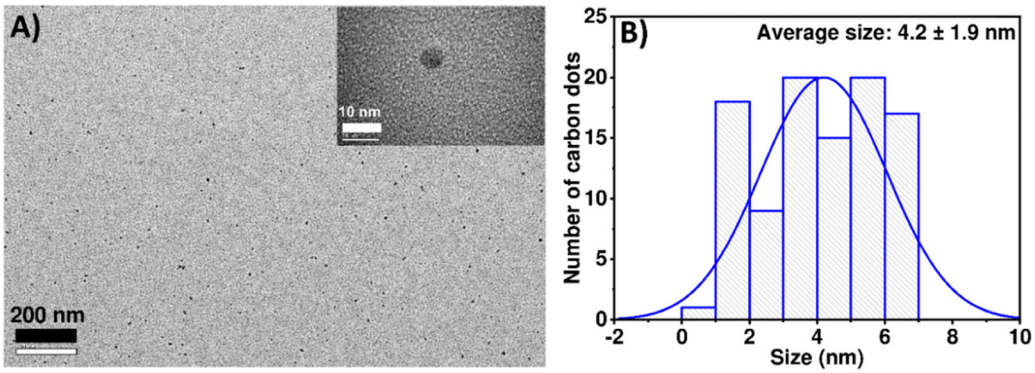

Fig. 1 (A) TEM image of CDs, scale bar: 200 nm. Inset displays the TEM image of a single CD with the scale bar as 10 nm. (B) Histogram showing the size distribution of CDs.

(Fig. S5C).[48] Moreover, the O 1s spectrum was deconvoluted into two peaks, revealing the presence of C–O (532.9 eV) and C═O (531.5 eV) (Fig. S5D).[40] These XPS results are in good agreement with FT-IR results.

3.3. Characterization of the UDC and CD-loaded QCS/OA hydrogel (UDC/CDs/H-Gel)

The hydrogel was formed by Schiff base-based crosslinking between amine groups of quaternized chitosan and aldehyde groups of oxidized alginates. Moreover, CDs were incorporated into the hydrogel along with the UDC drug to prepare the UDC/CDs/H-Gel. FT-IR spectroscopy was utilized to confirm the quaternization of amine groups present in chitosan and oxidation of alginate (Fig. S6 and S7). In the case of QCS, a new peak at 1480 cm^{-1} appeared, which was ascribed to the asymmetric C–H stretching of methyl groups of quaternary ammonium groups, along with all the peaks that were present in chitosan.[42] In the case of OA, a new peak at 1715 cm^{-1} appeared corresponding to the carbonyl of aldehyde groups formed after oxidation along with all the peaks that were present in alginate.[42] The FT-IR spectrum of UDC displayed the peaks at 3234 cm^{-1} (O–H stretching), 2928 cm^{-1} (C–H stretching), 1720 cm^{-1} (C═O stretching), and 1378 cm^{-1} (C–O stretching of carboxylic acid group) (Fig. S8).[12] Fig. 2 displays the comparative FT-IR spectra of QCS, OA, and UDC/CDs/H-Gel. The FT-IR spectrum of the UDC/CDs/H-Gel displayed the peaks at 3400 cm^{-1} (O–H and N–H stretching), 2926 cm^{-1} (C–H stretching), and 1633 cm^{-1} (C═N stretching). It showed the Schiff base-based crosslinking between amine groups of quaternized chitosan and aldehydic groups of oxidized alginate in the hydrogel layer. Electrostatic interactions and hydrogen bonding may additionally strengthen this Schiff base-based polymeric network established by chitosan and alginate. Here, the carboxyl and hydroxyl functional groups present on the surfaces of CDs and UDC can participate in electrostatic interaction and hydrogen bonding with the amine groups of chitosan and the carboxyl groups of alginate.

Furthermore, XPS analysis of the UDC/CDs/H-Gel was also carried out to confirm the chemical composition and Schiff base-based crosslinking in the hydrogel (Fig. S9). The XPS survey

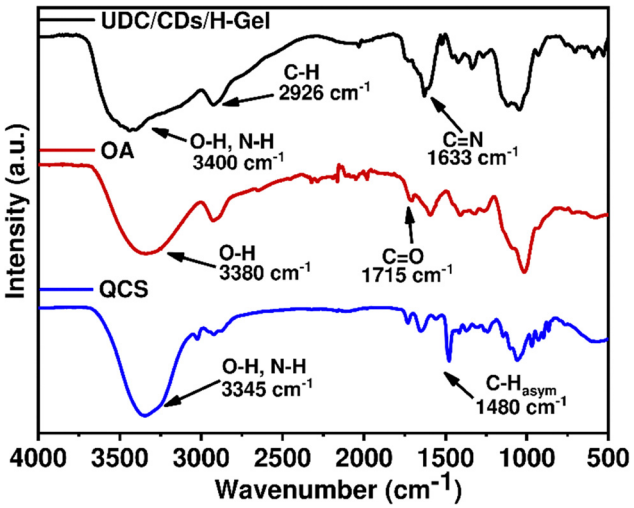

Fig. 2 Comparative FT-IR spectra of quaternized chitosan (QCS), oxidized alginate (OA), and the UDC/CDs/H-Gel.

spectrum of the UDC/CDs/H-Gel is presented in Fig. S9A in SI showing carbon, oxygen, and nitrogen peaks. The high resolution C 1s spectrum showed three peaks of O–C═O, C═N, and C–C with binding energies of 288 eV, 286.4 eV, and 284.7 eV, respectively (Fig. S9B).[47] The O 1s XPS spectrum consisted of two oxygen peaks (Fig. S9C). The peak at 532.5 eV was due to the O–C bond, and the peak at 530.9 eV was consistent with O═C.[47] Moreover, the N 1s spectrum presented two peaks upon deconvolution, which were related to $N(CH_3)_3^+$ and N═C with binding energies of 401.8 eV and 399.9 eV, respectively (Fig. S9D).[47] The fabricated UDC/CDs/H-Gel was also characterized using SEM and the results have been discussed later in Section 3.4.

3.4. Formation of the bilayer dressing (BL)

The bilayer dressing was prepared by using the vacuum filtration method that led to the formation of a strong interface between the two layers. Scanning electron microscopic analysis was carried out to examine the morphology of the bilayer dressing both on the surface and at the interface. As reported in the literature, immersion and coating approaches provide

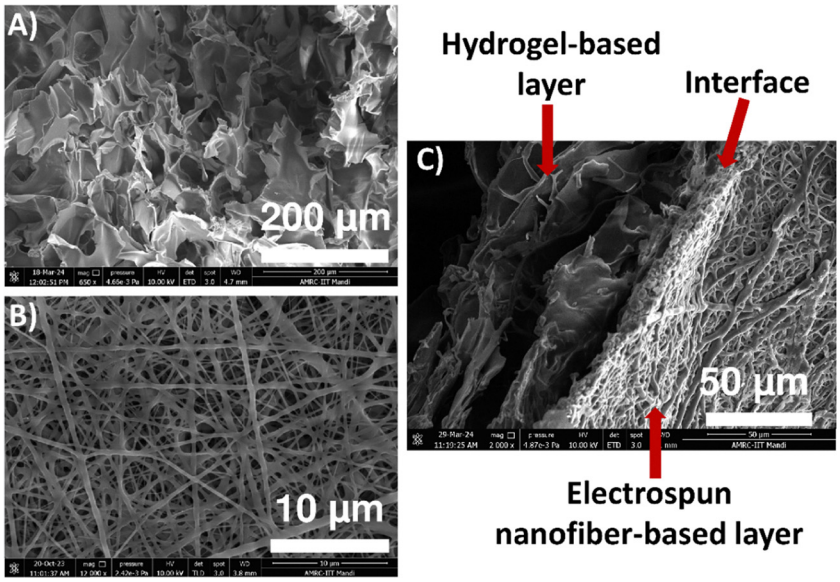

Fig. 3 SEM image of the bilayer dressing (BL). (A) Bottom UDC/CDs/H-Gel layer of the BL. Scale bar: 200 µm. (B) Top NF layer of the BL. Scale bar: 10 µm. (C) Interface between UDC/CDs/H-Gel and NF layers in the BL. Scale bar: 50 µm.

weak interfacial adhesion between the two layers, which may cause cracking.[49] In contrast, in the vacuum filtration process, the hydrogel forming solution is able to penetrate the pores of the nanofiber layer, which creates strong interfacial adhesion between hydrogel and nanofiber layers.[49] The porous morphology of the UDC/CDs/H-Gel layer can be easily seen in Fig. 3A. Furthermore, elemental mapping of the UDC/CDs/H-Gel confirmed that all the elements were evenly distributed across the hydrogel (Fig. S10). For comparison, SEM imaging and elemental mapping of the H-Gel were also carried out, revealing a porous morphology with a uniform elemental distribution throughout the hydrogel (Fig. S11). The morphology of the NF layer shown in Fig. 3B displayed the smooth and uniform surface of electrospun nanofibers, and the average diameter of nanofibers was 228 ± 61 nm (Fig. S12). The structural integrity of the bilayer matrix at the interface of hydrogel and NF layers was also observed by SEM (Fig. 3C).

3.5. Mechanical studies

Tensile strength and elongation at break were assessed to determine the influence of loading of CDs and UDC in the hydrogel layer (UDC/CDs/H-Gel). Furthermore, the impact of integrating the NF layer with the UDC/CDs/H-Gel layer on the mechanical behavior was also evaluated. A comparison of the tensile strength of the H-Gel, UDC/CDs/H-Gel, and BL is shown in Fig. 4A. It was observed that loading of CDs and UDC in the UDC/CDs/H-Gel led to an ~34% enhancement in tensile strength as compared to the unloaded H-Gel. The enhanced tensile strength can be correlated to the loaded material serving as a reinforcing filler. Additionally, the hydrogen bonding interactions of the carboxyl and hydroxyl groups of CDs and UDC with the amine groups of chitosan, as well as the carboxylic groups of alginate in the hydrogel layer, may further contribute to this enhancement in tensile strength. Similar findings have been reported by Kalaycıoğlu *et al.*[50]

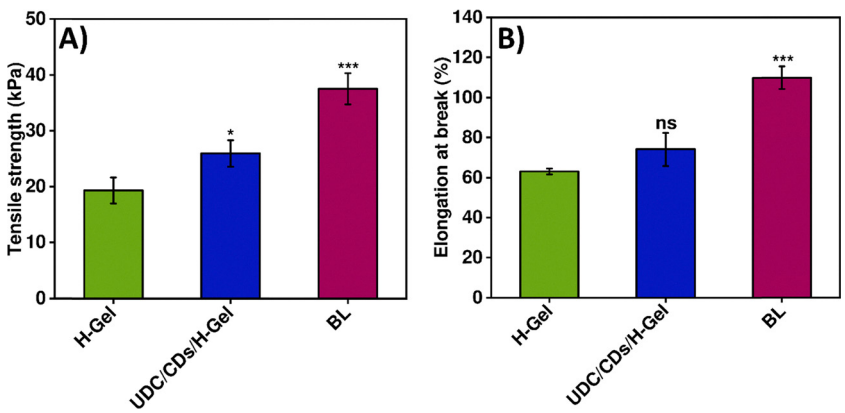

Fig. 4 Evaluation of mechanical properties. (A) Tensile strength of the H-Gel, UDC/CDs/H-Gel, and BL. (B) Elongation at break of the H-Gel, UDC/CDs/H-Gel, and BL. The data are expressed as mean ± standard deviation (n = 3), with significance levels indicated by p values <0.05 (*), 0.01 (**) and 0.001 (***).

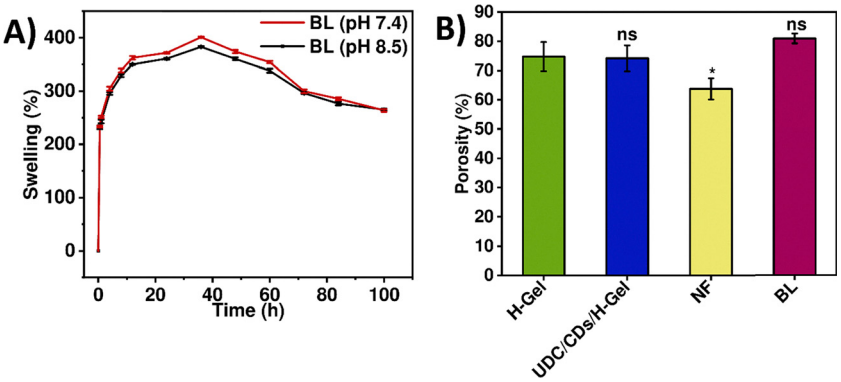

Fig. 5 (A) Swelling and degradation behavior of the BL at pH 7.4 and pH 8.5. (B) Porosity of H-Gel, UDC/CDs/H-Gel, NF, and BL. The data are expressed as mean ± standard deviation (n = 3), with significance levels indicated by p values <0.05 (*), 0.01 (**) and 0.001 (***).

Furthermore, integration of NF with the UDC/CDs/H-Gel layer led to ~45% increment in tensile strength. This enhancement could be due to the formation of an interpenetrating network at the interface of two layers, which was supported by the SEM image of the BL.[51] Elongation at break of the H-gel, UDC/CDs/H-Gel, and BL is shown in Fig. 4B. An ~17% increment was observed with the loading of CDs and UDC in the UDC/CDs/H-Gel layer as compared to the H-Gel. This increment can be attributed to CDs and UDC inhabiting the interchain gaps within the polymer network, thereby expanding the spacing between polymer chains. Comparable results have been reported by Riahi *et al.*[52] Additionally, the integration of nanofibers and hydrogel in the BL resulted in an ~48% increment in elongation at break. This increase may result from the entanglement of polymer chains at the interface of two layers, which can improve elongation at break, thereby aiding in withstanding the external forces.[53] For comparison, the mechanical strength of NF was measured separately, showing a tensile strength of 2.57 MPa and an elongation at break of 111% (Fig. S13).

3.6. Swelling and degradation studies

The swelling behavior of the H-Gel, UDC/CDs/H-Gel, NF, and BL was assessed in buffer solution of pH 7.4 and pH 8.5. These pH values were selected to represent the physiological environment (pH 7.4) and the alkaline conditions often associated with bacteria-infected wounds (pH 8.5).[54] Experimental results showed that the H-Gel and UDC/CDs/H-Gel displayed ~200% swelling in buffer solutions over 36 h (Fig. S14). With further incubation, hydrogels showed slight degradation. Additionally, the incorporation of CDs and UDC showed no significant impact on the swelling and degradation properties of the hydrogels. Similarly, NF also showed an increase in swelling at both pH 7.4 and pH 8.5 (Fig. S14). Initially, up to 12 h, the capacity of swelling was higher in the case of NF (~460% swelling) as compared to the H-Gel and UDC/CDs/H-Gel. Furthermore, nanofibers showed degradation with increase in incubation time. As displayed in Fig. 5A, the BL showed enhanced swelling behavior (~400% swelling in 36 h) at both pH 7.4 and pH 8.5 as compared to hydrogels. It was observed that the BL displayed degradation with increasing incubation time over 100 h.

These results highlight that NF exhibited the highest swelling over 12 h but degraded faster, whereas hydrogels showed the lowest swelling and maintained structural integrity longer than NF. Overall, the BL demonstrated intermediate swelling and degradation behavior as compared to its monolayer counterparts.

3.7. Porosity measurements

The ethanol displacement method was utilized to ascertain the porosity of the H-Gel, UDC/CDs/H-Gel, NF, and BL as ethanol cannot dissolve the lyophilized form of chitosan, alginate, and gelatin (Fig. 5B). It was observed that the porosity of the UDC/CDs/H-Gel was almost similar to that of the H-Gel, suggesting the negligible influence of CDs and UDC incorporated in the hydrogel layer. In the case of the BL, there was a slight increase in porosity with no significant difference with respect to hydrogels (Fig. 5B). Upon combining the nanofiber layer and hydrogel layer together, the interfacial interactions between them can introduce additional voids even if those layers were strongly bonded, as supported by the SEM image in Fig. 3. This architectural complexity may have allowed ethanol, used in the ethanol displacement method, to access more voids resulting in a slightly higher total porosity.

3.8. Contact angle measurements

The sessile drop method was employed to measure the water contact angle for evaluating surface wettability on both the sides of the BL, which influences cell adhesion and overall biocompatibility. The results showed that the water contact angles of the UDC/CDs/H-Gel layer side and the NF layer side were 63.2° and 58.5°, respectively, thus confirming the presence of the hydrophilic surface on both the sides of the BL (Fig. S15). Furthermore, the water contact angle of the UDC/CDs/H-Gel layer (58.5°) was lower as compared to the unloaded H-Gel (67.3°), which may be attributed to the hydrophilic nature of UDC.

3.9. *In vitro* UDC release from the UDC/CDs/H-Gel

UDC is a promising option for wound-healing applications due to its inhibition of NF-κB activation and its anti-inflammatory and tissue regeneration properties.[38,55] The *in vitro* release of

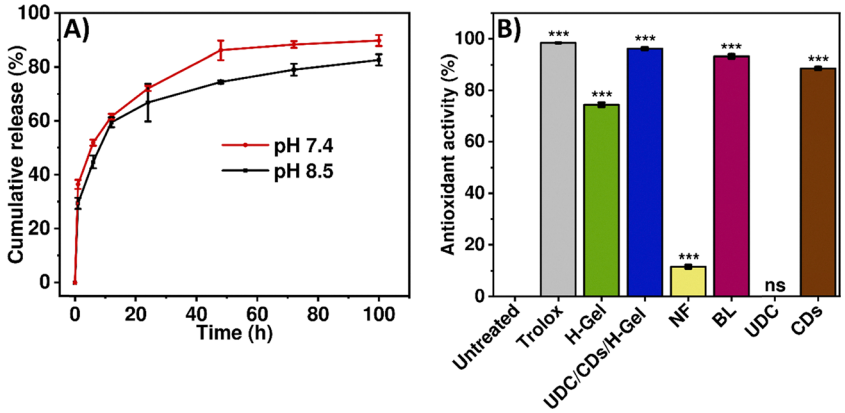

Fig. 6 (A) Release profiles of UDC from the UDC/CDs/H-Gel in PBS (pH 7.4 and pH 8.5). (B) Antioxidant activity of the H-Gel, UDC/CDs/H-Gel, NF, BL, UDC, and CDs, where the untreated DPPH radical solution was used as a negative control and Trolox was used as a positive control. The data are expressed as mean ± standard deviation (n = 3), with significance levels indicated by p values <0.05 (*), 0.01 (**) and 0.001 (***).

UDC from the UDC/CDs/H-Gel (loading efficiency = 10%) was studied at pH 7.4 and pH 8.5 over 100 h, and the samples were collected at regular intervals. The chosen pH values reflect the physiological environment (pH 7.4) and the alkaline conditions are often related to bacterial infections in wounds (pH 8.5).[54] The experimental results revealed that in the initial 10 h, 58% UDC was released at pH 7.4, while 54% UDC was released at pH 8.5. At the end of 100 h, the cumulative UDC release of 90% and 82% was achieved at pH 7.4 and pH 8.5, respectively (Fig. 6A). Higher UDC release at pH 7.4 can be ascribed to the increased number of protonated amine groups of chitosan, which in turn may influence the interaction of the UDC drug with the polymeric matrix of the hydrogel.[42]

Release of UDC was further analyzed using different release kinetics models and the highest correlation was observed with the Korsmeyer–Peppas model, indicating both diffusion and erosion-based release (Fig. S16 and Table S1).

3.10. Antioxidant activity

Excessive ROS levels may negatively impact the process of wound healing by extending the inflammatory phase.[56] Hence, it is important to eliminate these free radicals in order to foster efficient wound healing. It is notable that CDs present in the hydrogel layer, along with the lone pairs of hydroxyl and amine groups in the polymers, help in shielding cells from oxidative damage.[57]

In this regard, DPPH assay was used to check the antioxidant potential of the H-Gel, UDC/CDs/H-Gel, NF, BL, UDC, and CDs by measuring the extent of interaction between the sample and the purple-colored DPPH radical solution to form stable yellow-colored macromolecular radicals (Fig. 6B). Around 89% and 74% antioxidant activities were observed for CDs and the H-Gel, respectively. The antioxidant activity of the UDC/CDs/H-Gel (~96%) increased with the loading of CDs, which is in corroboration with the inherent antioxidant activity of bare CDs. The antioxidant activity of CDs can be primarily attributed to their functional groups (such as –OH, –COOH, –and NH_2).[58] Moreover, electron density on the carbon dot surface also helps in increasing antioxidant activity. As reported in the literature, from the mechanism perspective, this involves hydrogen atom transfer (HAT) and/or single electron transfer (SET) processes.[58] These features synergistically/additively contribute to efficient neutralization of radicals such as $DPPH^{\bullet}$.[58] Furthermore, the integration of NF with the UDC/CDs/H-Gel showed no discernible difference in the antioxidant activity of the BL (~93%).

3.11. Antibacterial activity

A quantitative assessment of antibacterial activity was done using the optical density (OD_{600}) method to evaluate the effect of the H-Gel, UDC/CDs/H-Gel, NF, BL, UDC, and CDs against *S. aureus* and *E. coli* (Fig. 7A and B). It is to be noted that the H-Gel by itself showed 58 and 60% antibacterial activity against *E. coli* and *S. aureus*, respectively. This intrinsic antibacterial behavior can be attributed to the interaction of the positively charged quaternary amine group of quaternized chitosan with negatively charged phosphatidylglycerol moieties residing in bacterial membranes.[59] Furthermore, the UDC/CDs/H-Gel showed 81 and 69% antibacterial activity against *E. coli* and *S. aureus* respectively. The enhanced efficacy of the UDC/CDs/H-Gel can be ascribed to the additive effect of positively charged quaternized chitosan and CDs incorporated inside the film. The antibacterial activity of CDs can be ascribed to their interaction with the bacterial cell walls, leading to the distortion of the bacterial membrane.[60] On the other hand, NF showed 41 and 51% antibacterial activity against *E. coli* and *S. aureus*, respectively, owing to the presence of amine groups present in gelatin and chitosan. Furthermore, the integration of both hydrogel and NF layers in the BL led to a substantial increase in its antibacterial activity. The BL showed 92 and 88% antibacterial activity against *E. coli* and *S. aureus* respectively, within 24 h.

The antibacterial behavior of BL was further supported by live–dead staining of *S. aureus* and *E. coli* (Fig. 7C and D). SYTO 9 and propidium iodide (PI) were used to stain bacterial cells that had been treated with the BL for 24 h. PI preferably combines with the DNA of cells exhibiting compromised membrane integrity and emits red fluorescence. In cells with

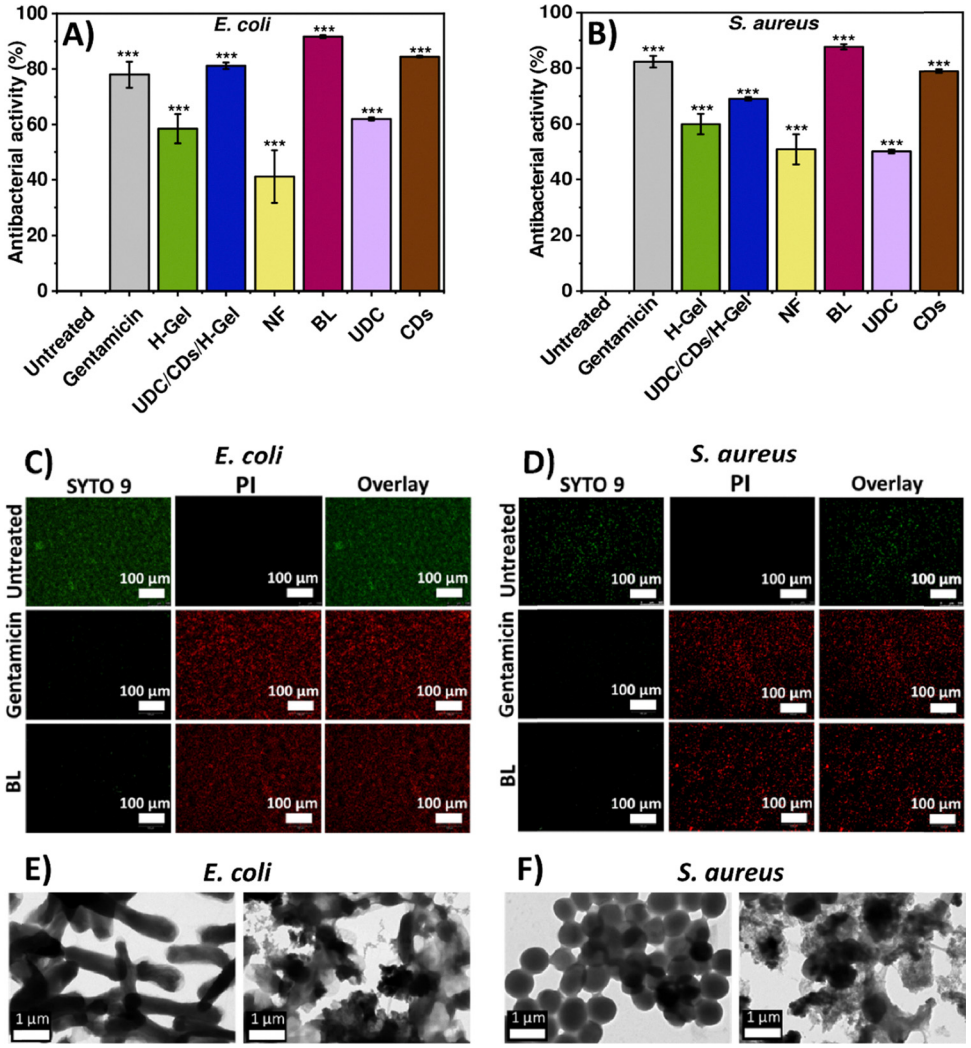

Fig. 7 Antibacterial activity of the H-Gel, UDC/CDs/H-Gel, NF, BL, UDC, and CDs against (A) *E. coli*, and (B) *S. aureus*. Live–dead assay of (C) *E. coli* and (D) *S. aureus*. Scale bar: 100 µm. Here, untreated bacteria were used as a negative control and gentamicin sulphate-treated bacteria were used as a positive control. TEM analysis to examine the antibacterial mechanism: (E) untreated *E. coli* and *E. coli* treated with the BL and (F) untreated *S. aureus* and *S. aureus* treated with the BL. Scale bar: 1 µm. The data are expressed as mean ± standard deviation (n = 3), with significance levels indicated by p values <0.05 (*), 0.01 (**) and 0.001 (***).

intact membranes, SYTO 9 interacts with both DNA and RNA, resulting in green fluorescence, which indicates viable cells. The experimental results showed that untreated bacterial cells displayed green fluorescence confirming live cells, whereas bacterial cells treated with the BL exhibited red fluorescence. Here, the decrease in green fluorescence and the increase in red fluorescence indicated a significantly higher percentage of dead cells in BL-treated bacteria as compared to the control sample consisting of untreated bacteria.

Furthermore, TEM analysis (Fig. 7E and F) was employed to examine the antibacterial mechanism of the BL against both *S. aureus* and *E. coli*. Here, untreated bacterial cells maintained their structural integrity, with the cell membrane remaining intact. Conversely, BL treatment caused evident disruptions in the bacterial cell membranes, leading to the leakage of cytoplasmic content and finally resulting in cell death.

3.12. Cell viability studies

MTT assay was utilized to compare the viability of murine fibroblast cells (L929) after treatment with the H-Gel, UDC/CDs/H-Gel, NF, BL, UDC, and CDs (Fig. 8). It was observed that the H-Gel, UDC/CDs/H-Gel, and NF exhibited a cell viability of ~102, ~97, and ~108%, respectively, whereas UDC and CDs showed a cell viability of ~140 and ~43%, respectively. Furthermore, the BL demonstrated a significantly enhanced cell viability of ~130%, surpassing the individual monolayer counterparts. It is to be noted that in addition to similar cell viability as UDC, the BL also offers additional benefits, such as antioxidant and antibacterial activity, which is useful for effective wound healing.

Moreover, live–dead assay was carried out to compare the cytocompatibility of the H-Gel, UDC/CDs/H-Gel, NF, BL, UDC, and CDs (Fig. 9). Untreated cells were utilized as a control.

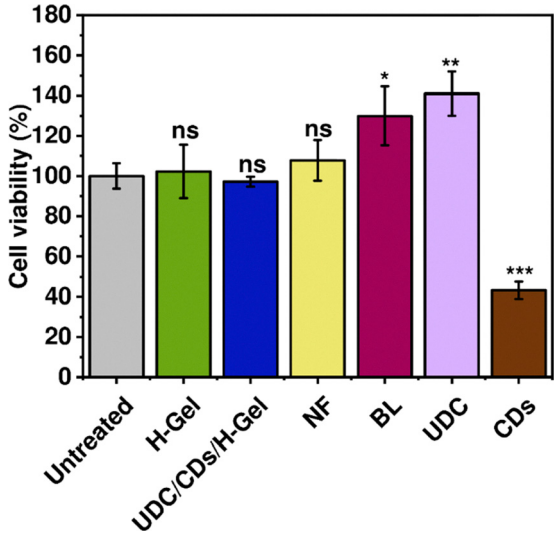

Fig. 8 Cell viability studies of murine fibroblast (L929) cells treated with the H-Gel, UDC/CDs/H-Gel, NF, BL, UDC, and CDs, where untreated cells were utilized as a control. The data are expressed as mean ± standard deviation (n = 3), with significance levels indicated by p values <0.05 (*), 0.01 (**) and 0.001 (***).

Here, ethidium homodimer-1 and calcein AM were used together for cell staining. Ethidium homodimer-1 selectively binds to dead cells, producing a red fluorescence, while calcein H-Gel, UDC/CDs/H-Gel, and NF showed good cell viability. However, the UDC/CDs/H-Gel also showed the presence of a few dead cells as compared to the H-Gel, which may be attributed to the presence of CDs. Notably, the BL showed excellent cell viability, as confirmed by a high density of live cells and no visible dead cells. Additionally, the BL mitigates the impact of CDs, thus ensuring a favorable environment for enhanced cell viability and proliferation as compared to its monolayer counterparts. The exact mechanism by which the BL accomplishes increase in cell viability is not yet clear, but it may be related to physical obstructions within the system.[61] This further supported the MTT assay results and validated the cytocompatibility and cell proliferating nature of the BL.

In addition to the extract-based cytocompatibility assessment, direct cell culture studies on the both sides of the BL were also carried out. This experiment confirmed that, after 24 h, both surfaces supported cell adhesion, indicating the material's suitability for direct cell–material interaction (Fig. S17). Notably, the NF showed relatively higher cell adhesion as compared to the UDC/CDs/H-Gel. The NF offers a robust structure that promotes efficient cell adhesion and the presence of a gelatin matrix concurrently provides a bioactive environment that promotes cell adhesion. Similar results have been reported by Ramanathan *et al.*[35]

3.13. ROS scavenging studies

H_2DCFDA assay was carried out to examine the ROS scavenging ability of the H-Gel, UDC/CDs/H-Gel, NF, BL, UDC, and CDs in H_2O_2-treated L929 cells (Fig. 10). Cell-permeable H_2DCFDA undergoes deacetylation by cellular esterases, resulting in the

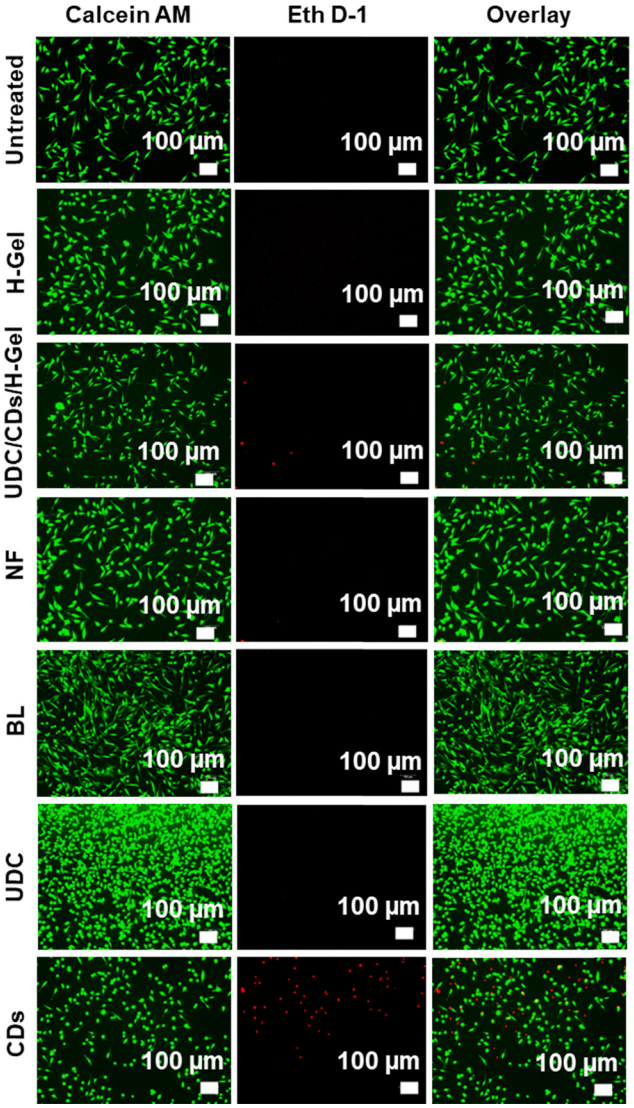

Fig. 9 Live–dead images of murine fibroblast (L929) cells treated with the H-Gel, UDC/CDs/H-Gel, NF, BL, UDC, and CDs, where untreated cells were utilized as a control. Scale bar: 100 µm.

formation of 2′,7′-dichlorodihydrofluorescein. Upon exposure to ROS, it is rapidly oxidized into highly fluorescent 2′,7′-dichlorofluorescein.[57] To assess the ROS scavenging ability of the test samples, the cells were first exposed to H_2O_2 to induce ROS generation. Subsequently, these ROS induced cells were treated with desired samples. Here, untreated cells (without any exposure to H_2O_2) were used as a control, which showed a fluorescence intensity of ~2000. The H_2O_2-treated cells showed a significantly higher fluorescence intensity of ~13 412, thus confirming the substantial ROS generation. The experimental results showed that H-Gel treated cells exhibited a fluorescence intensity of ~4000, indicating substantial ROS scavenging. This can be ascribed to the presence of quaternized chitosan in the hydrogel matrix that caused a significant increase in the capability of ROS neutralization, which is notably higher than pure chitosan.[62,63]

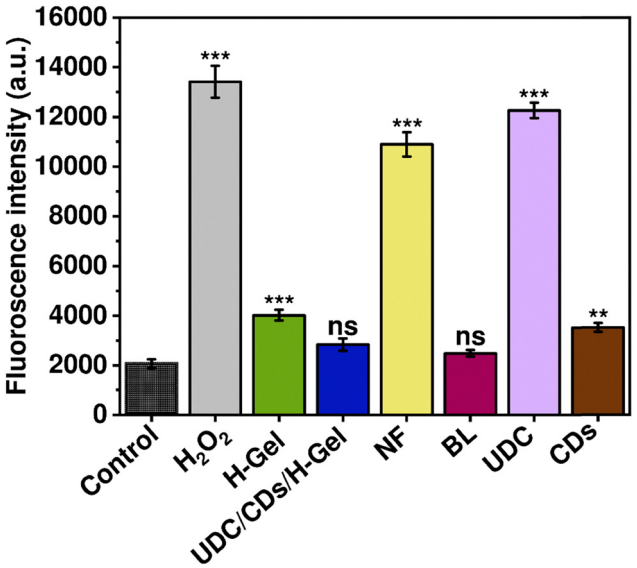

Fig. 10 ROS scavenging analysis of the H-Gel, UDC/CDs/H-Gel, NF, BL, UDC, and CDs in H_2O_2-treated murine fibroblast (L929) cells, where untreated cells were utilized as a control. The data are expressed as mean ± standard deviation (n = 3), with significance levels indicated by p values <0.05 (*), 0.01 (**) and 0.001 (***).

UDC/CDs/H-Gel-treated cells showed improved ROS scavenging ability, lowering the fluorescence intensity further to ~3000, which can be correlated to the antioxidant activity of CDs. In contrast, NF-treated cells showed an increase in fluorescence intensity (~11 000), thus showing poor ROS scavenging behavior. Although chitosan present in NF contains amine groups that can interact with ROS, its scavenging ability may not be sufficient to effectively neutralize ROS. Similar observations have been reported by Wu *et al.*[64] Among the test samples, UDC-treated cells displayed the highest fluorescence intensity (~12 000), demonstrating its minimal scavenging potential, whereas CD treated cells showed relatively better ROS scavenging ability with a fluorescence intensity of ~3500. Notably, BL-treated cells showed a discernible decrease in fluorescence intensity (~2400), which is very close to the control and significantly lower than H_2O_2-treated cells. This highlights the excellent ROS scavenging ability of the BL and the obtained findings are in accordance with the antioxidant studies conducted employing DPPH assay.

3.14. Hemolysis assay

RBCs are indicative of the body's overall response to the treatment.[65] Hence, hemocompatibility of the H-Gel, UDC/CDs/H-Gel, NF, BL, UDC, and CDs was assessed using hemolysis assay. The experimental results indicated that the test samples caused minimal disruption to RBCs. Here, CDs showed a maximum hemolysis of ~6% and the BL showed minimum hemolysis (~4.5%), whereas Triton-X (positive control) treated RBCs resulted in crimson color solution attributed to the complete lysis of RBCs (Fig. S18). The percentage of hemolysis for the BL was less than 5%, adhering to the acceptable threshold for biomaterials.[4]

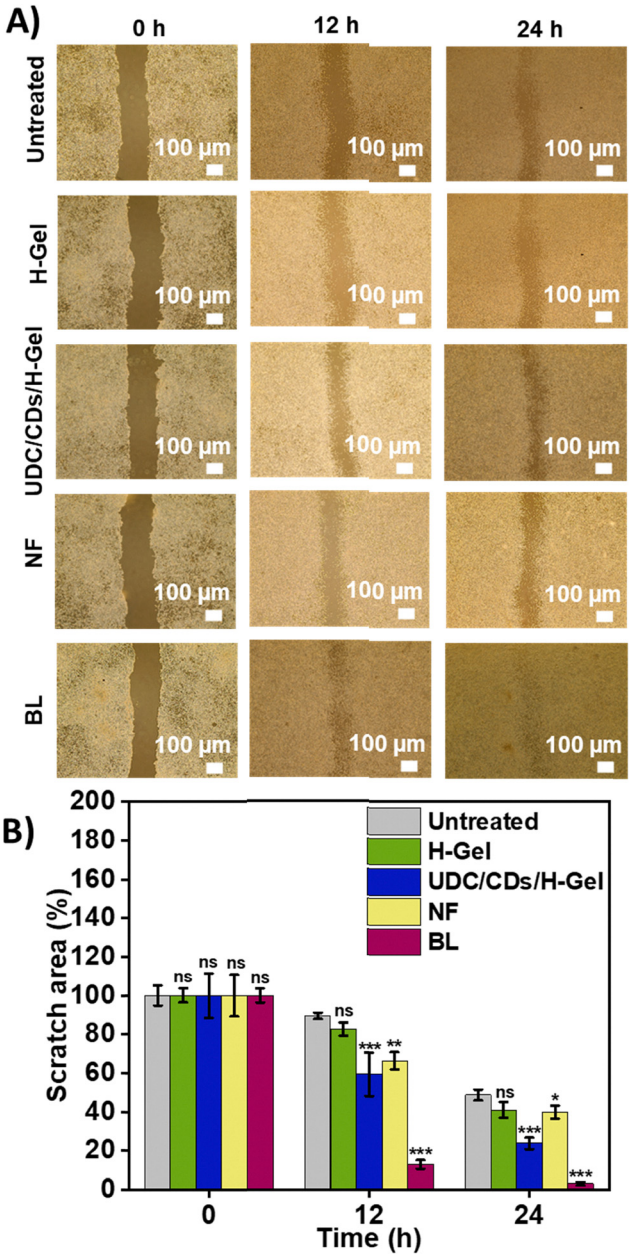

Fig. 11 *In vitro* wound healing using murine fibroblast (L929) cells. (A) Scratch images in the case of the H-Gel, UDC/CDs/H-Gel, NF, and BL for 0, 12, and 24 h. Scale bar: 100 µm. (B) Quantitative estimation of the wound closure in the case of the NF, H-Gel, UDC/CDs/H-Gel, and BL. Here, untreated cells were utilized as a control. The data are expressed as mean ± standard deviation (n = 3), with significance levels indicated by p values <0.05 (*), 0.01 (**) and 0.001 (***).

3.15. Hemostatic activity

To evaluate the hemostatic potential of the H-Gel, UDC/CDs/H-Gel, NF, BL, UDC, and CDs, the whole blood clotting test was performed considering untreated blood as a control. It involves measuring the absorbance of hemoglobin in uncoagulated blood. The reduced absorbance of hemoglobin signifies increased immobilization of RBCs by the material, consequently leading to enhanced clot formation.[42] It was observed

Table 1 Comparative analysis of different wound healing matrices reported in the literature with the current study

S. no.	System	Antioxidant activity	Antibacterial activity	Cell viability	ROS scavenging ability	Hemostatic behavior	*In vitro* wound closure	Ref.
1.	Oxytetracycline loaded lignin/chitosan/polyvinyl alcohol-based hydrogel	39.27%	ZOI: 22 mm for *E. coli* and 24.5 mm for *S. aureus*	~85% (L929)	—	—	7.2% cell migration in 4 h (L929)	Preet *et al.*[66]
2.	Glucose oxidase and catalase nanoenzyme–chitosan hydrogel	—	OD_{600}: ~78% for *E. coli* and ~95% for *S. aureus*	~110% (L929 and HUVECs)	Yes	—	38.37% (L929) and 74.12% (HUVECs) cell migration in 24 h	Li *et al.*[67]
3.	Carboxymethyl chitosan/tannic acid/Cu^{2+} based hydrogel	—	CCM: 100% for methicillin-resistant *S. aureus* death in 12 days	~90% (HEK and HUVECs)	—	—	~95% wound closure (HEK) after 6 h	Lin *et al.*[68]
4.	Photocatalytic graphene nanocomposite and curcumin loaded chitosan/polyvinyl alcohol-based hydrogel	—	ZOI: 18 mm for *E. coli*, 17 mm for *P. aeruginosa*, 16 mm for *S. aureus*, and 15 mm for *E. faecalis*	~98% (NIH3T3)	—	Yes	~99% wound closure (NIH3T3) after 48 h	Jayabal *et al.*[69]
5.	Poly glycerol sebacate/poly lactide acid/platelet-rich plasma electrospun nanofibers	—	—	~100% (L929, HUVEC, and RAW-264.7)	—	—	~99% wound closure (L929) after 24 h	Heydari *et al.*[70]
6.	BL	~93%	OD_{600}: 92% for *E. coli* and 88% for *S. aureus*	~130% (L929)	Yes	Yes	~97% wound closure	Current study

ZOI: zone of inhibition; CCM: colony counting method.

that among all the test groups, the BL and UDC/CDs/H-Gel showed maximum reduction in the hemoglobin absorbance value in comparison to untreated blood, which may be attributed to the additive effect of the polymer matrix, UDC, and CDs (Fig. S19). The results obtained in our study are comparable to the reported literature by Xia *et al.*[4]

3.16. Scratch assay

Scratch assay was performed to examine the *in vitro* wound healing capability of the BL and its monolayer counterparts (Fig. 11A). In this regard, a scratch was made on the monolayer of cells followed by incubation with test samples. Untreated cells were utilized as a control here. To monitor the healing, images were taken at 0, 12, and 24 h using a microscope. Quantitative analysis of the scratch area using ImageJ software revealed the wound closure capability of different test samples (Fig. 11B). After 24 h, an ~49% unhealed scratch area was noted in the case of untreated cells. Among the tested monolayer counterparts, the UDC/CDs/H-Gel showed the highest wound closure efficiency, with the ~24% unhealed scratch area after 24 h. On the other hand, the NF and H-Gel showed similar levels of healing with the ~40% unhealed scratch area after 24 h. Interestingly, scratch treated with the BL exhibited a faster wound closure with only ~3% unhealed scratch area after 24 h. This clearly indicates the enhanced effectiveness of the BL for wound healing by significantly outperforming both the untreated group and the monolayer counterparts.

A comparative analysis of the current study with previously reported studies in the literature is shown in Table 1.

4. Conclusions

Herein, a bilayer dressing (BL) was developed, which mimics the dermal and epidermal architecture of normal skin by integrating an electrospun nanofiber-based layer (NF) with a hydrogel layer loaded with the ursodeoxycholic drug (UDC) and carbon dots (CDs). The BL was imparted with multiple active features like antioxidant, antibacterial, hemostasis, and reactive oxygen species (ROS) scavenging ability for enhanced wound healing. The BL exhibited remarkable swelling behavior and porosity as compared to the hydrogel layer. Additionally, the integration of the nanofiber-based layer with the hydrogel layer in the BL led to a significant enhancement in the tensile strength and elongation at break, thereby demonstrating its improved mechanical behavior. The BL showed excellent antioxidant activity (~93%) and antibacterial activities against *E. coli* (92%) and *S. aureus* (88%). Cell viability studies, including MTT and live–dead assay, demonstrated enhanced cell viability in the case of the BL as compared to individual NF and hydrogel layers. Furthermore, the BL outperformed its monolayer counterparts by displaying excellent hemocompatibility and enhanced wound closure, thus opening a new pathway for the healing of infectious wounds.

Author contributions

D. B.: data curation and analysis, writing an initial version of the manuscript, and figure preparation; V. C.: data curation for biological studies; V. N.: data curation; Y. T.: data curation; Y. S.: supervision of biological studies and editing of the manuscript; G. A.: conceptualization, supervision, and manuscript preparation.

Conflicts of interest

The authors declare no conflict of interest.

Data availability

Data available within the article or its SI. See DOI: https://doi.org/10.1039/d5tb00800j

Acknowledgements

GA thanks the financial support from ANRF Science & Engineering Research Board (SERB-ANRF), India (Grant No. WEA/2023/000001). VC is thankful to the Ministry of Education for the Prime Minister Research Fellowship (PMRF, Application No. PMRF-192002-167) and YS is thankful to DST/GITA India-Taiwan S&T Cooperation Program – Call for Proposal 2021 (grant # GITA/DST/TWN/P-98/2022) for the financial assistance.

References

1 Y. Cheng, X. Liu, F. Fan, Y. Zhang, M. Cao, L. Bai, H. Ming, H. Chen, Y. Liu and Y. Yu, *Biomater. Sci.*, 2025, **13**, 758–776.
2 Q. Lu, X. Tang, B. Tao, K. Huang, K. Li, C. Liu, B. Gao, M. Xu, W. Geng, K. Li and F. Zhou, *Int. J. Biol. Macromol.*, 2025, **296**, 139685.
3 Y. Wang, C. Chen, C. He, W. Dong, X. Yang, Q. Kong, B. Yan and J. He, *Carbohydr. Polym.*, 2025, **348**, 122865.
4 Y. Xia, S. Yan, H. Wei, H. Zhang, K. Hou, G. Chen, R. Cao and M. Zhu, *ACS Appl. Mater. Interfaces*, 2024, **16**, 34578–34590.
5 A. Sood, M. S. Granick and N. L. Tomaselli, *Adv. Wound Care*, 2013, **3**, 511–529.
6 G. D. Winter, *Nature*, 1962, **193**, 293–294.
7 Y. Liang, J. He and B. Guo, *ACS Nano*, 2021, **15**, 12687–12722.
8 X. Zhang, Y. Liang, S. Huang and B. Guo, *Adv. Colloid Interface Sci.*, 2024, **332**, 103267.
9 C. Cheng, R. Wang, J. Ma, Y. Zhang, Q. Jing and W. Lu, *Int. J. Biol. Macromol.*, 2024, **267**, 131237.
10 A. Bužarovska, J. P. Stanoeva, P. Karamanolevski, A. D. Popa, S. Dinescu and L. Avérous, *J. Appl. Polym. Sci.*, 2025, **142**, e56708.
11 D. Jafari, M. Gholipourmalekabadi, S. Alizadeh, M. Rajabi Fomeshi, M. Amoupour and A. Samadikuchaksaraei, *Artif. Organs*, 2024, **48**, 117–129.
12 D. Bhardwaj, R. Bhaskar, A. K. Sharma, M. Garg, S. S. Han and G. Agrawal, *ACS Appl. Bio Mater.*, 2024, **7**, 879–891.
13 H. Zhang, X. Lin, X. Cao, Y. Wang, J. Wang and Y. Zhao, *Bioact. Mater.*, 2024, **33**, 355–376.
14 J. Li, Y. Li, C. Guo and X. Wu, *Chem. Eng. J.*, 2024, **481**, 148458.
15 H. S. Zayed, S. Saleh, A. E. Omar, A. K. Saleh, A. Salama and E. Tolba, *Int. J. Biol. Macromol.*, 2024, **261**, 129665.
16 C. Hong, H. Chung, G. Lee, D. Kim, Z. Jiang, S.-H. Kim and K. Lee, *Biomacromolecules*, 2024, **25**, 4344–4357.
17 T. Long, T. Xu, R. Li, Z. Xu, D. Li, C. Mu, L. Yuan and Y. Mu, *Int. J. Biol. Macromol.*, 2024, **254**, 127918.
18 Y. W. Ding, Z. W. Zhang, X. Y. Cui, R. Y. Hu, Y. Li, S. D. Huang, S. Q. Du, J. W. Dao and D. X. Wei, *Chem. Eng. J.*, 2025, **503**, 158387.
19 Y. Li, Y. Wang, Y. Ding, X. Fan, L. Ye, Q. Pan, B. Zhang, P. Li, K. Luo, B. Hu, B. He and Y. Pu, *ACS Nano*, 2024, **18**, 17251–17266.
20 W. Luo, Z. Li, J. Che, X. Li, H. Zhang, J. Tian, C. Wang, G. Y. Li and L. Jin, *ACS Appl. Mater. Interfaces*, 2024, **16**, 34720–34731.
21 A. Martorana, M. Lenzuni, M. Contardi, F. S. S. Palumbo, S. Cataldo, A. Pettignano, V. Catania, D. Schillaci, M. Summa, A. Athanassiou, C. Fiorica, R. Bertorelli and G. Pitarresi, *ACS Appl. Mater. Interfaces*, 2024, **16**, 20186–20201.
22 H. Jiang, L. Li, Z. Li and X. Chu, *Biomed. Microdevices*, 2024, **26**, 12.
23 M. W. Pletts and R. E. Burrell, *Wound Repair Regen.*, 2025, **33**, e13249.
24 S. A. Althawab, T. Alsulami, H. Alzahrani and A. Alzahrani, *Colloids Surf., A*, 2024, **698**, 134554.
25 R. Chandrasekaran, U. Ushani, G. Sankar, J. Joseph, K. Natarajan, S. Palani, P. Sridhar, R. Nagaraj and S. Sagadevan, *Bionanoscience*, 2025, **15**, 1–21.
26 S. Zaffar, S. Saha, T. Agrawal, S. K. Gupta, P. Gulati, D. Paul, A. Verma, S. Pal and T. Rakshit, *ACS Biomater. Sci. Eng.*, 2025, **11**, 4219–4230.
27 L. Qu, S. Zhao, Q. Chang, Y. Xie, J. Wang and X. Deng, *ACS Appl. Nano Mater.*, 2025, **8**, 9044–9054.
28 L. Li, Y. Wang, S. Hu, X. Chang, Q. Ding, K. Wang, Y. Chen and J. Zheng, *Acta Biomater.*, 2025, **195**, 467–478.
29 M. Rahmati, J. J. Blaker, S. P. Lyngstadaas, J. F. Mano and H. J. Haugen, *Mater. Today Adv.*, 2020, **5**, 100051.
30 M. Mirhaj, M. Tavakoli, J. Varshosaz, S. Labbaf, S. Salehi, A. Talebi, N. Kazemi, V. Haghighi and M. Alizadeh, *Carbohydr. Polym.*, 2022, **292**, 119648.
31 W. Cao, D. Xia, L. Zhou, Y. Liu, D. Wang, C. Lianga and M. Chen, *Mater. Today Phys.*, 2024, **40**, 101316.
32 M. Tavakoli, M. Mirhaj, J. Varshosaz, M. H. Al-Musawi, Y. Q. Almajidi, A. M. Danesh Pajooh, M. Shahriari-Khalaji, F. Sharifianjazi, M. Alizadeh and S. Labbaf, *ACS Appl. Mater. Interfaces*, 2023, **15**, 55276–55286.
33 M. Zhang, S. Gong, K. Hakobyan, Z. Gao, Z. Shao, S. Peng, S. Wu, X. Hao, Z. Jiang and E. H. Wong, *Adv. Sci.*, 2024, **11**, 2309006.
34 B. Lombardi, C. Casale, G. Imparato, F. Urciuolo and P. A. Netti, *Adv. Healthcare Mater.*, 2017, **6**, 1601422.
35 G. Ramanathan, L. S. Seleenmary Sobhanadhas, G. F. Sekar Jeyakumar, V. Devi, U. T. Sivagnanam and P. Fardim, *Biomacromolecules*, 2020, **21**, 2512–2524.
36 N. Chundayil Kalathil, M. R. Shah, V. C. Lailakumari, P. Prabhakaran, H. Kumarapilla and G. S. V. Kumar, *ACS Appl. Bio Mater.*, 2024, **7**, 6492–6505.
37 A. Eskandarinia, M. Gharakhloo, P. K. Kermani, S. Navid, M. A. Salami, D. Khodabakhshi and A. Samadi, *Carbohydr. Polym.*, 2023, **319**, 121171.
38 P. Li, Z. Chen, K. Meng, Y. Chen, J. Xu, X. Xiang, X. Wu, Z. Huang, R. Lai, P. Li, Z. Lai, X. Ao, Z. Liu, K. Yang, X. Bai and Z. Zhang, *Orthop. Surg.*, 2024, **16**, 183–195.
39 S. M. Galal, S. M. El Kiki and E. M. Elgazzar, *Cell Biochem. Funct.*, 2024, **42**, e70024.
40 Y. Zhang, Z. Li, L. Sheng and A. Meng, *Colloids Surf., A*, 2023, **657**, 130580.
41 J. Sun, W. Jia, J. Guo, N. K. Khanzada, P. Jin, P. W. Wong, X. Zhang and A. K. An, *Desalination*, 2022, **533**, 115742.

42 D. Negi and Y. Singh, *ACS Appl. Nano Mater.*, 2023, **6**, 13616–13628.
43 A. Dhiman, A. K. Sharma, D. Bhardwaj and G. Agrawal, *Int. J. Biol. Macromol.*, 2023, **228**, 323–332.
44 A. Sood, A. Gupta, R. Bharadwaj, P. Ranganath, N. Silverman and G. Agrawal, *Carbohydr. Polym.*, 2022, **294**, 119833.
45 K. Fukada, T. Tajima and M. Seyama, *ACS Appl. Mater. Interfaces*, 2021, **13**, 59006–59011.
46 N. Vladislavić, I. Š. Rončević, M. Buzuk, M. Buljac and I. Drventić, *J. Solid State Electrochem.*, 2021, **25**, 841–857.
47 M. Kehrer, J. Duchoslav, A. Hinterreiter, M. Cobet, A. Mehic, T. Stehrer and D. Stifter, *Plasma Processes Polym.*, 2019, **16**, 1800160.
48 B. B. Campos, C. Abellán, M. Zougagh, J. Jimenez-Jimenez, E. Rodríguez-Castellón, J. C. G. Esteves da Silva, A. Ríos and M. Algarra, *J. Colloid Interface Sci.*, 2015, **458**, 209–216.
49 M. Zhang, S. Xu, C. Du, R. Wang, C. Han, Y. Che, W. Feng, C. Wang, S. Gao and W. Zhao, *Colloids Surf., B*, 2023, **222**, 113119.
50 Z. Kalaycıoğlu, E. Torlak, G. Akın-Evingür, İ. Özen and F. B. Erim, *Int. J. Biol. Macromol.*, 2017, **101**, 882–888.
51 X. He, S. Wang, J. Zhou, D. Zhang, Y. Xue, X. Yang, L. Che, D. Li, S. Xiao and S. Liu, *ACS Appl. Mater. Interfaces*, 2022, **14**, 4579–4587.
52 Z. Riahi, A. Khan, J.-W. Rhim, G. H. Shin and J. T. Kim, *Int. J. Biol. Macromol.*, 2024, **258**, 129302.
53 J. Liu, P. Miao, W. Zhang, G. Song, J. Feng, X. Leng and Y. Li, *Polymer*, 2022, **256**, 125254.
54 H. Haidari, K. Vasilev, A. J. Cowin and Z. Kopecki, *ACS Appl. Mater. Interfaces*, 2022, **14**, 51744–51762.
55 T. Milivojac, M. Grabež, A. Krivokuća, U. Maličević, M. Gajić Bojić, Đ. Đukanović, S. Uletilović, N. Mandić-Kovačević, T. Cvjetković, M. Barudžija, N. Vojinović, A. Šmitran, L. Amidžić, M. P. Stojiljković, M. Čolić, M. Mikov and R. Škrbić, *Mol. Cell. Biochem.*, 2025, **480**, 563–576.
56 C. Huang, Z. Zhang, Y. Fang, K. Huang, Y. Zhao, H. Huang and J. Wu, *Int. J. Biol. Macromol.*, 2024, **278**, 134496.
57 V. Chawla, S. Sharma and Y. Singh, *ACS Biomater. Sci. Eng.*, 2023, **9**, 2647–2662.
58 N. Sharma, A. Sharma and H. J. Lee, *Environ. Chem. Lett.*, 2025, **23**, 1061–1109.
59 Y. Gong, H. Wang and J. Sun, *Biomacromolecules*, 2024, **25**, 4619–4638.
60 J. Hua, P. Hua and K. Qin, *Colloids Surf., A*, 2024, **680**, 132672.
61 T. Wang, Y. Li, Y. Liu, Z. Xu, M. Wen, L. Zhang, Y. Xue and L. Shang, *J. Colloid Interface Sci.*, 2023, **633**, 851–865.
62 R. Song, Z. Zhong and L. Lin, *Int. J. Biol. Macromol.*, 2016, **85**, 102–110.
63 F. Luan, L. Wei, J. Zhang, W. Tan, Y. Chen, F. Dong, Q. Li and Z. Guo, *Molecules*, 2018, **23**, 516.
64 Y. Wu, Q. Wu, X. Fan, L. Yang, L. Zou, Q. Liu, G. Shi, X. Yang and K. Tang, *J. Biomed. Mater. Res., Part A*, 2024, **112**, 1532–1547.
65 M. Yin, S. Wan, X. Ren and C.-C. Chu, *ACS Appl. Mater. Interfaces*, 2021, **13**, 14688–14699.
66 J. Preet, K. Pathania, J. Kaur, R. Singh, D. B. Salunke and S. V. Pawar, *Mater. Adv.*, 2024, **5**, 9445–9457.
67 Z. Li, X. Fan, Z. Luo, X. J. Loh, Y. Ma, E. Ye, Y.-L. Wu, C. He and Z. Li, *Nanoscale*, 2022, **14**, 14970–14983.
68 J. Lin, S. Li, Y. Ying, W. Zheng, J. Wu, P. Wang and X. Liu, *ACS Omega*, 2024, **9**, 4386–4394.
69 P. Jayabal, V. Kannan Sampathkumar, A. Vinothkumar, S. Mathapati, B. Pannerselvam, S. Achiraman and G. D. Venkatasubbu, *ACS Appl. Bio Mater.*, 2023, **6**, 615–627.
70 P. Heydari, A. Zargar Kharazi and L. Shariati, *Sci. Rep.*, 2024, **14**, 12019.